Multirate Estimation and Control of Body Slip Angle for Electric Vehicles Based on Onboard Vision System

Yafei Wang, *Student Member, IEEE*, Binh Minh Nguyen, *Student Member, IEEE*, Hiroshi Fujimoto, *Senior Member, IEEE*, and Yoichi Hori, *Fellow, IEEE*

***Abstract*—A new method for vehicle body-slip-angle estimation using nontraditional sensor configuration and system model is proposed, which enables robust estimation against vehicle parameter uncertainties. In this approach, a linear vehicle bicycle model is augmented with a simple visual model. As the visual model contains few uncertain parameters and increases the observer's design freedom, the combined model-based estimator provides more accurate estimation result compared with the traditional bicycle-model-based one. However, two issues are raised by the combined vehicle and vision models: 1) image processing introduces delay in the visual measurements, and 2) the sampling time of a normal camera is much longer than that of other onboard sensors. For electric vehicles, the control period of motors is much shorter than the sampling time of a normal camera. Considering the aforementioned delay and multirate problems, a multirate Kalman filter with intersample compensation is designed, and the estimation performance can be improved during the sampling intervals of the vision system. Then, a two-degree-of-freedom controller is designed using the estimated body slip angle as feedback for reference tracking. With the proposed multirate estimator, the controller achieves better tracking performance than the single-rate method. The effectiveness of the proposed estimator and controller is demonstrated by both simulations and experiments.**

***Index Terms*—Body slip angle, electric vehicle (EV), measurement delay, multirate estimation, vehicle motion control, vision system.**

Nomenclature

a_x	Longitudinal acceleration rate.
d_r	Track width.
r	Wheel radius.
l_f	Distance from the center of gravity (CoG) to front axle.
l_{pre}	Preview distance.
l_r	Distance from CoG to rear axle.
m	Vehicle mass.
y_{cg}	Lateral offset at CoG.
y_l	Lateral offset at the preview point.
C_f	Front tire cornering stiffness.
C_r	Rear tire cornering stiffness.
F_{rl}	Longitudinal force acting on the rear left tire.
F_{rr}	Longitudinal force acting on the rear right tire.
I	Moment of inertia about the yaw axis.
N_z	Yaw moment generated by differential forces.
T_l	Rear left in-wheel motor (IWM) torque.
T_r	Rear right IWM torque.
V_{cg}	Vehicle's velocity at CoG.
V_x	Vehicle's longitudinal velocity at CoG.
V_y	Vehicle's lateral velocity at CoG.
β	Body slip angle.
γ	Yaw rate.
δ_f	Front-steering angle.
ψ	Vehicle heading angle.

Manuscript received September 25, 2012; revised January 7, 2013 and March 4, 2013; accepted April 22, 2013. Date of publication June 27, 2013; date of current version August 9, 2013.

The authors are with the Department of Advanced Energy, Graduate School of Frontier Sciences, The University of Tokyo, Chiba 277-8561, Japan (e-mail: wang@hori.k.u-tokyo.ac.jp; minh@hori.k.u-tokyo.ac.jp; fujimoto@k.u-tokyo.ac.jp; hori@k.u-tokyo.ac.jp).

Color versions of one or more of the figures in this paper are available online at http://ieeexplore.ieee.org.

Digital Object Identifier 10.1109/TIE.2013.2271596

I. Introduction

BODY SLIP angle, also known as sideslip angle, is considered as one of the key enablers of vehicle motion control systems [1]–[4]. However, off-the-shelf products for body-slip-angle measurement such as noncontact optical sensor and GPS-based apparatus are very expensive for practical applications [2]. Therefore, cost-effective methods for vehicle body-slip-angle estimation have been studied extensively during the last few decades [2]–[6]. Based on the models used, past research can be generally divided into two categories: kinematic-model-based and dynamic-model-based methods. In [3], the body slip angle was calculated based on its kinematic relationship with the yaw rate, longitudinal acceleration, and so on; however, this method involves integration of sensor signals and therefore requires high-precision sensors. Given that the kinematic model does not include time-varying parameters such as tire cornering stiffness, the driving condition change has little influence on the estimation accuracy. However, this method is heavily affected by sensor noise and drift [4]. The second method is based on vehicle dynamics with either linear or nonlinear bicycle model. In [5], linear-bicycle-model-based observers were constructed and verified with experimental data. To provide more design freedom, lateral acceleration was utilized as an additional measurement in [4], but uncertainties (cornering stiffness) are also brought into the system observation equation. Although the linear observer is easy to use, the parameters of the linear models are fixed; thus, not all driving conditions can be addressed [2]. Considering the nonlinear characteristics of tires, nonlinear-model-based methodologies provide better estimation accuracy under different driving conditions compared with the linear one [6]. However, such nonlinear estimators are very complex [2].

Meanwhile, look-ahead cameras have increasingly become popular in vehicles. Most related studies focus on lane keeping and collision avoidance [7]. Nevertheless, investigating other applications using the onboard vision system is desirable. This paper investigates a vision-based body-slip-angle estimation method, and the visual model is independent of the uncertain parameters of the vehicle. Moreover, vehicle position measurement from the vision system is very accurate [7]. Therefore, incorporating visual information can increase the estimator's design freedom without introducing uncertainties into it. However, two issues arise with this method. The first one is visual measurement delay due to image processing, and it is generally too long to be neglected. Furthermore, as the sampling time of the normal camera is much longer than that of the other onboard sensors, fusing these signals presents a multirate issue. For the measurement delay, various methods such as lifting method and interpolation have been proposed [8], [9]. For the multirate problem, a straightforward solution is to down-sample fast-rate sensors to adapt slower device and then construct a single-rate estimator [10]. In this application, gyroscope and encoders can be sampled every 33 ms to fit the sampling period of the camera. For electric vehicles (EVs), one of their advantages is the millisecond-level sampling time of the motors, and this merit has been utilized for high-performance motion control systems [1]. Here, if the single-rate estimator is employed, the sampling rates between the state feedback and the control input cannot match. Moreover, an impulsive behavior is introduced if the control frequency is decreased to adapt the rate of the feedback loop. To update the system states during intersampling, several multirate Kalman filters were built for industrial applications [11], [15]. Nevertheless, the outputs of such estimators are not smooth because of the loss of residual information during intersampling.

In this paper, a simple linear model that combines the vehicle and vision models is utilized, and it enables robust estimation against changes in vehicle parameters. To solve the delay and multirate issues, a multirate Kalman filter that takes into account the intersample residual and measurement delay is constructed. Then, with the estimated body slip angle, a two-degree-of-freedom (2DOF) controller is designed for body-slip-angle manipulation. The remainder of this paper is organized as follows. In Section II, vehicle and visual models are introduced, and the multirate and delay issues are explained in detail. In Section III, experimental setups are briefly introduced. In Section IV, a single-rate Kalman filter, a multirate Kalman filter without intersample compensation, and the proposed multirate Kalman filter with intersample estimation are built for body-slip-angle estimation. A body-slip-angle controller is designed with the estimators in Section V. In Section VI, simulation and experimental results that demonstrate the effectiveness of the proposed methods are shown. Finally, conclusions are presented in Section VII.

II. System Modeling and Problem Statement

A. Combined Vehicle and Vision Models

Vehicle Model: For state estimation and control, the vehicle bicycle model is usually employed because of its simplicity

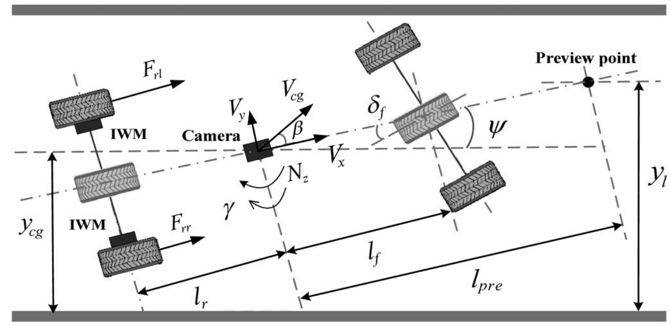

Fig. 1. Combined vehicle and vision models.

[13], [14]; for EVs with IWMs, the differential torque generated by the left and right wheels should also be included in the model. The governing equations are given in (1) and (2), where N_z is used as control input in this research. Detailed derivations can be found in [2].

$$m \cdot V_x \cdot (\dot{\beta} + \gamma) = 2 \cdot C_f \cdot \left(\delta_f - \frac{l_f}{V_x}\gamma - \beta\right) + 2 \cdot C_r \cdot \left(\frac{l_r}{V_x}\gamma - \beta\right) \quad (1)$$

$$I \cdot \dot{\gamma} = 2 \cdot l_f \cdot C_f \cdot \left(\delta_f - \frac{l_f}{V_x}\gamma - \beta\right) - 2 \cdot l_r \cdot C_r \cdot \left(\frac{l_r}{V_x}\gamma - \beta\right) + N_z. \quad (2)$$

As IWMs can generate positive and negative torques easily, a simple torque distribution law (TDL) can be defined as

$$\begin{aligned} T_l &= F_{rl} \cdot r = \frac{m \cdot r \cdot a_x}{2} + \frac{r \cdot N_z}{d_r} \\ T_r &= F_{rr} \cdot r = \frac{m \cdot r \cdot a_x}{2} - \frac{r \cdot N_z}{d_r}. \end{aligned} \quad (3)$$

Vision Model: The vehicle model is independent of road reference, whereas the vision model is obtained from the geometric relationship between the vehicle and the road. The vision model is also shown in Fig. 1. The gray borders in Fig. 1 are lane makers, and the camera is located at the vehicle's CoG. In this model, assumptions that the vehicle travels along a straight road and that the onboard vision system detects the lane and provides relative position information were made.

To derive the vision model, ψ and β are assumed to be small [10]. Based on Fig. 1, y_l is approximated as

$$\begin{aligned} y_l &= y_{cg} + l_{\text{pre}} \cdot \sin\psi \\ &\approx y_{cg} + l_{\text{pre}} \cdot \psi. \end{aligned} \quad (4)$$

Then, y_{cg} is derived as follows based on geometry:

$$\begin{aligned} \dot{y}_{cg} &= V_{cg} \cdot \sin(\beta + \psi) \\ &= V_x / \cos(\beta) \cdot \sin(\beta + \psi) \\ &\approx V_x \cdot (\beta + \psi). \end{aligned} \quad (5)$$

The final equation that describes the body slip angle, yaw rate, and heading angle is obtained by taking the derivative of

(3) and substituting (5) into it

$$\dot{y}_l = V_x \cdot \beta + l_{\mathrm{pre}} \cdot \gamma + V_x \cdot \psi. \tag{6}$$

Heading angle ψ can be simply modeled as the integration of the yaw rate as

$$\dot{\psi} = \gamma. \tag{7}$$

Although curved roads are not considered here, the system can still be modeled in the same manner by taking the curvature into account.

Combined System Model: Combining (1)–(7) yields a new system that is represented in a continuous state space form as (8). The first two states are modeled by the vehicle model, and the latter two are modeled by the vision model. Clearly, the vision model contains much fewer uncertainties compared with the bicycle model. In the combined vehicle and vision models, the measurable outputs are yaw rate, vehicle heading angle, and lateral offset at the preview point

$$\begin{aligned} \dot{x} &= A \cdot x + B \cdot u \\ y &= C \cdot x \end{aligned} \tag{8}$$

where

$$x = [\beta \quad \gamma \quad \psi \quad y_l]^{\mathrm{T}} \qquad u = [\delta_f \quad N_z]^{\mathrm{T}}$$

$$y = [\gamma \quad \psi \quad y_l]^{\mathrm{T}}$$

$$A = \begin{bmatrix} -\frac{2(C_f+C_r)}{mV_x} & -1-\frac{2(C_f l_f - C_r l_r)}{mV_x^2} & 0 & 0 \\ -\frac{2(C_f l_f - C_r l_r)}{I} & -\frac{2\left(C_f l_f^2 + C_r l_r^2\right)}{IV_x} & 0 & 0 \\ 0 & 1 & 0 & 0 \\ V_x & l_{\mathrm{pre}} & V_x & 0 \end{bmatrix}$$

$$B = \begin{bmatrix} \frac{2C_f}{mV_x} & \frac{2C_f l_f}{I} & 0 & 0 \\ 0 & \frac{1}{I} & 0 & 0 \end{bmatrix}^{\mathrm{T}} \qquad C = \begin{bmatrix} 0 & 1 & 0 & 0 \\ 0 & 0 & 1 & 0 \\ 0 & 0 & 0 & 1 \end{bmatrix}.$$

B. Multirate and Delayed Measurements

To apply the Kalman filter in real time, (8) needs to be implemented in the discretized form, as shown in (9), where k is the time step. As the system model contains uncertainties and the sensor measurements are contaminated by noises, process noise w_k and measurement noise v_k are also included in (9). Moreover, the state space matrices are time varying because of changes in vehicle parameters.

$$\begin{aligned} x_{k+1} &= G_k \cdot x_k + H_k \cdot u_k + w_k \\ y_k &= C_k \cdot x_k + v_k \end{aligned} \tag{9}$$

where

$$G_k = e^{A \cdot T} \qquad H_k = \int_0^{\mathrm{T}} e^{A \cdot \tau} \cdot B d\tau$$

$$C_k = C, \qquad T: \text{sampling time}.$$

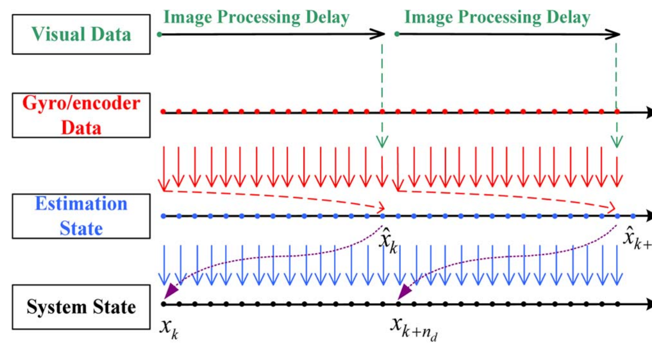

Fig. 2. System time sequence diagram.

In the combined model, two different measurement times are available: The sampling period of yaw rate is short (defined as T_s), and the updating time of visual information is much longer (defined as T_l). Therefore, the selection of T_s and T_l for system discretization needs to be considered. If the system sampling time is set to T_l, data from the high-speed sensors have to be dropped during intersampling of the slow-speed device. This is a straightforward solution for the multirate issue but obviously deteriorates the estimation performance. An alternative method is to set the system sampling time to T_s; then, all the information from the fast-rate sensors can be utilized. However, the intersample residuals of the slow-speed device must be addressed.

Moreover, measurements from the vision system are delayed because of image processing. In fact, the image processing time varies, depending on the incoming images and hardware loads. In this paper, for the convenience of postprocessing, a constant image processing time is implemented in the image processing program, as described later in this paper. Therefore, the visual output equation becomes (10), where $n_d = T_d/T_s$ and T_d is the time delay. The sampling sequence is shown in Fig. 2

$$y_k^{\mathrm{vis}} = C_{k-n_d}^{\mathrm{vis}} \cdot x_{k-n_d}^{\mathrm{vis}} + v_{k-n_d}^{\mathrm{vis}}. \tag{10}$$

Unlike normal measurements, the information from the visual system is captured at step $k - n_d$ but is only available at step k. Therefore, the whole system's output equation is expressed as

$$y_k = \begin{bmatrix} C_k^{veh} & O \\ O & C_{k-n_d}^{\mathrm{vis}} \end{bmatrix} \cdot \begin{bmatrix} x_k^{veh} \\ x_{k-n_d}^{\mathrm{vis}} \end{bmatrix} + \begin{bmatrix} v_k^{veh} \\ v_{k-n_d}^{\mathrm{vis}} \end{bmatrix}. \tag{11}$$

Two interpretations can be drawn for the delay: 1) The visual information is delayed n_d steps with the fast data as the reference, and 2) the visual information is delayed by one step with itself as the reference. Given that the multirate ratio between the fast and slow sensors is generally high, the order of the state space equation using the lifting method can become large [12]. Thus, solving the delay issue using the second interpretation that can simplify the estimator design is desirable. Notably, although the system multiplicity (N) can be reduced by increasing T_s, lifting approaches are still not practical. Because T_s cannot be set large enough in consideration of control performance [20], in other words, N cannot be reduced to be small enough for implementation of lifting method.

(a)

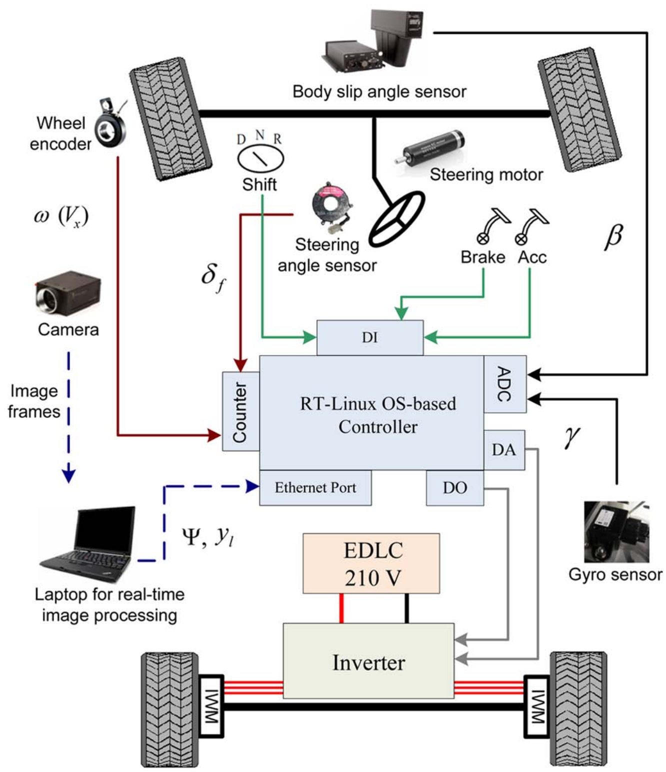

(b)

Fig. 3. Experimental vehicle and its structure. (a) Experimental EV. (b) Overall structure.

TABLE I
SPECIFICATIONS OF THE EXPERIMENTAL VEHICLE

Item	Description
Vehicle Parameters	
Total mass (m)	380 kg
Distance from CoG to front axle (l_f)	0.8 m
Distance from CoG to rear axle (l_r)	0.6 m
Tread at rear axle (d_r)	0.82 m
Wheel radius (r)	0.22 m
Front tire cornering stiffness (C_f)	6,000 N/rad
Rear tire cornering stiffness (C_r)	6,000 N/rad
Yaw moment of inertial (I_z)	136.08 N·m/(rad/s^2)
Maximum torque of IWM	100 N·m
Sensor Configurations	
Gyro/acceleration integrated Sensor	Nissan EWTS53BC
Steering angle sensor	Nissan 47945-AS500
Wheel encoder	Aisin AW
Acceleration pedal sensor	Toyota Auto Body
Brake on/off sensor	Toyota Auto Body
Body slip angle sensor	CORRSYS-DATRON S-400
Onboard camera	Point Grey GRAS-03K2M
Control System	
Inverter	Myway (PWM Vector Control)
Sampling time	0.001 s
Operation system	Real-time Linux
Control computer	PC104 board, A/D board, D/A board, Counter board

III. EXPERIMENTAL SETUP

The experimental vehicle used in this research is a single-seat EV with IWMs, as shown in Fig. 3(a). The prototype is produced by Toyota Auto Body Company, Ltd., and it was modified for studies related to capacitor and motion control. The vehicle's specification is given in Table I.

The vehicle structure and sensor configurations are shown in Fig. 3(b). In this vehicle, 28 electric double-layer capacitor modules with a total voltage of 210 V were installed, and they were directly connected to an inverter to drive the two IWMs attached in the rear wheels. The maximum speed of this vehicle can reach up to 45 km/h. For the steering system, a Maxon dc motor was installed to drive the front-steering shaft, and it can operate with steer-by-wire function. A PC104 embedded computer with real-time Linux system was employed for vehicle control, and the control program was configured to run at a speed of 1 ms/cycle. Based on the measured and estimated vehicle state information, the controller calculates the desired torques in real time and gives the commands to the inverter for torque generation. For vehicle state measurement and estimation, several sensors were installed. An accelerometer/gyro-integrated sensor was installed in the vehicle's CoG to provide longitudinal acceleration and yaw rate information. A steering angle sensor was attached to the steering shaft to detect the steering angle and direction. Wheel speed encoders were installed in the front wheels (nondriven wheels) to acquire the vehicle velocity. To evaluate the estimation results, S-400, a noncontact optical sensor produced by Corrsys-Datron, was installed for online body-slip-angle acquisition. The onboard vision system includes a Grasshopper camera produced by Point Grey and a laptop computer for image processing. The camera was installed at the top of the vehicle with a tilt angle of 8° and a preview distance of 5.135 m. Considering that normal onboard cameras have a sampling rate of 30 Hz, the frame rate of the camera was set to 30 fps. The images captured by the camera were grabbed by a CARDBUS frame grabber in the laptop and then processed by the image processing program in real time. The image processing software was implemented in C ++ with OpenCV and Point Grey Research's libraries, and the image processing time was designed to be constant (30 ms) for the benefit of data postprocessing. That is, the visual information is only updated every 33 ms and is delayed for one visual sampling step. The image processing was based on effective algorithms such as Laplacian of Gaussian and Random Sample Consensus; it can detect normal roads with straight lane markers and outputs ψ and y_l to the vehicle controller based on the User Datagram Protocol. Further explanation of the image processing techniques and the vision system can be found in [22].

IV. Body-Slip-Angle Estimation Based on the Combined Vehicle and Vision Models

In this section, the body-slip-angle observer is designed based on the combined system model.

A. Augmentation of Delayed Measurements

As aforementioned, two issues need to be considered in the observer design, namely, delayed and multirate measurements. In this paper, the time-delay problem is solved using the lifting method, and the basic idea is to include the delayed states into the state space equation [8], [9].

First, the information from the vision system is considered to have a one-step delay, as discussed in Section II. Equation (12) is then defined as

$$\overline{\psi}_{k+1} = \psi_k \qquad \overline{y}_{l_{k+1}} = y_{l_k}. \tag{12}$$

To include the delayed visual information, the state of the combined system model is augmented using (12) as additional states.

Finally, the new discretized system is defined by the following equation, and the current visual states can then be estimated with the Kalman filter (will be introduced in the next section) using the previous one-step information:

$$\begin{aligned} x^a_{k+1} &= G^a_k \cdot x^a_k + H^a_k \cdot u_k + w_k \\ y^a_k &= C^a_k \cdot x^a_k + v_k \end{aligned} \tag{13}$$

where

$$x^a_k = [\,\beta_k \quad \gamma_k \quad \psi_k \quad y_{l_k} \quad \overline{\psi}_k \quad \overline{y}_{l_k}\,]^{\mathrm{T}}$$

$$y^a_k = [\,\gamma_k \quad \overline{\psi}_k \quad \overline{y}_{l_k}\,]^{\mathrm{T}} \qquad u_k = [\,\delta_{f_k} \quad N_{z_k}\,]^{\mathrm{T}}$$

$$G^a_k = \begin{bmatrix} G_k & O_{4\times 2} \\ O_{2\times 2} \quad I_{2\times 2} & O_{2\times 2} \end{bmatrix} \qquad H^a_k = [\,H^{\mathrm{T}}_k \quad O_{2\times 2}\,]^{\mathrm{T}}$$

$$C^a_k = \begin{bmatrix} 0 & 1 & 0 & 0 & 0 & 0 \\ 0 & 0 & 0 & 0 & 1 & 0 \\ 0 & 0 & 0 & 0 & 0 & 1 \end{bmatrix}.$$

The next step is to solve the multirate issue. Two kinds of solutions can be adopted, namely, single-rate and multirate Kalman filters.

B. Design of Single-Rate Kalman Filter

To solve the problem of sampling mismatch, one simple method is to adapt the sampling rate of high-speed sensors to the slowest device [10]. In this paper, the system sampling time was set to adapt to the camera (i.e., T was set to 33 ms) and to combine the sampling rates of the gyroscope and camera. Then, the data from the gyroscope are ignored during the camera's intersampling. After the sampling rate adaptation, the next design steps are the same as those of the normal Kalman filter, which can be found in the literature [9]. Basically, the Kalman filter consists of time update, measurement update, and Kalman gain calculation. The Kalman filter principle is shown in Fig. 4, where Q and R are the covariance matrices for the process and measurement noises as defined in (14). The two matrices (Q and R) could change at each time step; however, for implementation convenience, they are usually assumed in practice as constant

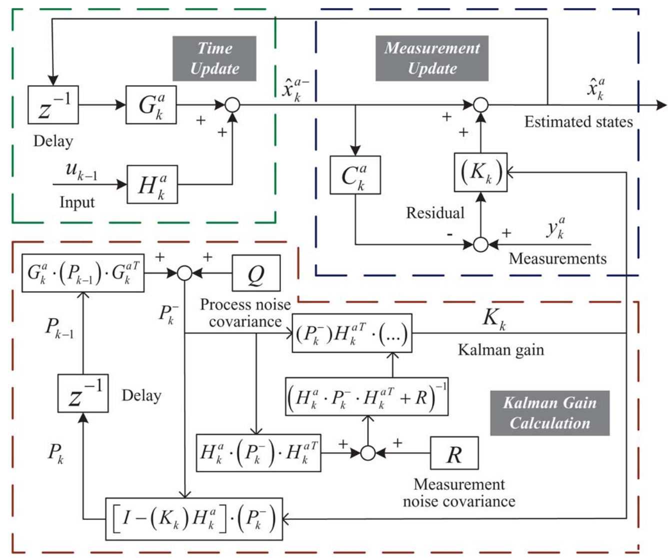

Fig. 4. Operating principle of the Kalman filter.

$$Q = E\left[w_k w^{\mathrm{T}}_k\right] \qquad R = E\left[v_k v^{\mathrm{T}}_k\right]. \tag{14}$$

The estimated state of the single-rate Kalman filter is expressed in the form of (15), where n is an integer. This estimator is only updated at the speed of the slowest device.

$$\hat{x}^a_k = \hat{x}^{a-}_k + K_k \cdot \left(y^a_k - C^a_k \cdot \hat{x}^{a-}_k\right), \quad \text{only when } k = n\cdot(T_l/T_s). \tag{15}$$

Although the traditional Kalman filter can be simply employed to solve the multirate issue by considering the sampling rate adjustment, other problems arise. Based on the viewpoint of sensor fusion, measurements from high-sampling-rate sensors cannot be fully utilized, resulting in deterioration of estimation accuracy. Moreover, the estimated body slip angle is only updated every 33 ms, which is not fast enough for the high-performance motion control of EVs.

C. Design of Multirate Kalman Filter

The multirate Kalman filter is aimed at utilizing more information from high-speed sensors and increasing the updating rate of the estimator for high-performance control. First, the system is discretized with the sampling time of the fastest device (T is set to 1 ms in this research). Next, the time and measurement updates need to be designed. For the time update, the multirate Kalman filter can be implemented in the same way as the single-rate one. The camera's sampling period is T_l. During the time intervals of $n \cdot T_l$, no information from the vision system is available. Therefore, pseudocorrections have to be implemented for the operation of the measurement update. An intuitive solution is to assume that the measurements from the vision system are exactly the same as those of the model-based predictions [15]. Using this method, corrections can still be made with information from high-speed sensors during the intersampling of the slow-rate device. In this application, the corrections of the Kalman filter are based on the yaw rate measured by the gyro sensor during the intersampling periods of the vision system. The states estimation equation is shown as

$$\hat{x}_k^a = \hat{x}_k^{a-} + K_k \cdot \left(\tilde{y}_k^a - C_k^a \cdot \hat{x}_k^{a-}\right) \tag{16}$$

where

$$\tilde{y}_k^a = \begin{cases} \left[\gamma_k, \overline{\psi}_k, \overline{y}_{l_k}\right]^{\mathrm{T}}, & \text{if } k = n \cdot (T_l/T_s) \\ \left[\gamma_k, \overline{\psi}_k^-, \overline{y}_{l_k}\right]^{\mathrm{T}}, & k \neq n \cdot (T_l/T_s). \end{cases}$$

By assuming that the measurements of the slow-rate sensors are the same as the model-based predictions during the intersampling periods, the aforementioned method realizes faster updating frequency than the single-rate one. However, this assumption is not true in practice because of the presence of modeling errors. In addition, the convergence of such method is questionable during intersampling periods, as shown in the Appendix. Therefore, the intersample residuals must be computed for better estimation accuracy and convergence.

The basic idea of the intersample residual estimation is to utilize the residual of the initial step that is available and propagate it to the following intermeasurement steps. After T_d/T_s steps, the residual is recalculated when new measurements come in. The general definition of residual ε and estimation error e are shown in the following equations, respectively,

$$\varepsilon = y - C \cdot \hat{x}^- \tag{17}$$

$$e = x - \hat{x}. \tag{18}$$

To derive the pseudoresidual algorithm, process noise w_k and measurement noise v_k are assumed to be small and are hence ignored. This assumption is based on two considerations. First, the intersample residual compensation in this application is designed for visual information. As aforementioned, the vision model and the visual measurements are assumed to be accurate. Second, obtaining w_k and v_k in real time for algorithm implementation is difficult.

Based on the discrete system in (9), the algorithm for the intersample residual calculation can be generalized in four steps as follows.

1) When sensor measurements are available, the initial residual at step k is obtained as (19). The initial residual is available at each $n \cdot T_l$ step.

$$\varepsilon_k = y_k - C \cdot \hat{x}_k^-. \tag{19}$$

2) Using (18) and considering that matrix C might not be invertible, the initial estimation error can be estimated as

$$e_k = \left[(C^{\mathrm{T}} \cdot C)^{-1} \cdot C^{\mathrm{T}} - K_k\right] \cdot \varepsilon_k. \tag{20}$$

3) From the definition of the estimation error in (18), the estimation dynamics at step $k+j$ can be propagated using the following equation, where $j \in [1, T_l/T_s)$:

$$\begin{aligned} e_{k+j} &= x_{k+j} - \hat{x}_{k+j} \\ &= x_{k+j} - \hat{x}_{k+j}^- - K_{k+j} \cdot \left(y_{k+j} - C \cdot \hat{x}_{k+j}^-\right) \\ &= \left(x_{k+j} - \hat{x}_{k+j}^-\right) - K_{k+j} \cdot \left(C \cdot x_{k+j} - C \cdot \hat{x}_{k+j}^-\right) \\ &= (I - K_{k+j} \cdot C) \cdot G_{k+j-1} \cdot e_{k+j-1}. \end{aligned} \tag{21}$$

4) Finally, the pseudoresidual during the intersampling period is given by the following equation, and it is updated using (21):

$$\begin{aligned} \tilde{\varepsilon}_{k+j} &= y_{k+j} - C \cdot \hat{x}_{k+j}^- = C \cdot x_{k+j} - C \cdot \hat{x}_{k+j}^- \\ &= C \cdot G_{k+j} \cdot e_{k+j-1}. \end{aligned} \tag{22}$$

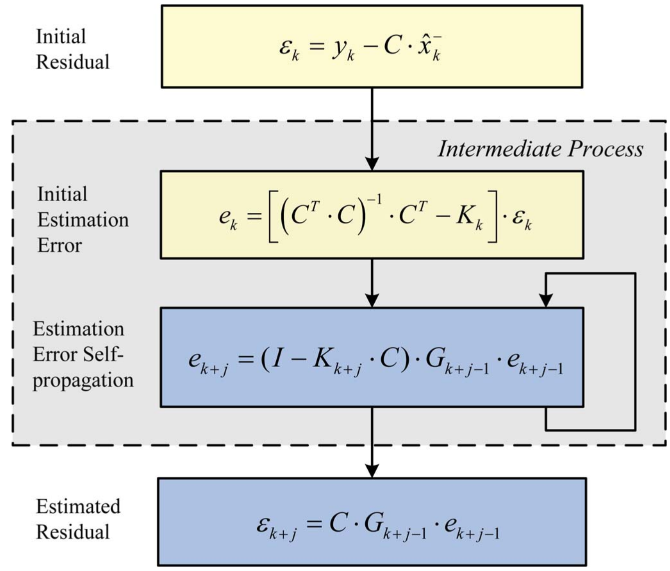

Fig. 5. Operating principle of the intersample residual estimation.

The aforementioned four steps are shown in Fig. 5. The first two steps are the initialization, and the estimation error is then self-propagated using (21). Finally, the intersample residuals are obtained using the estimated error dynamics. The estimation errors must be noted to be unknown in reality because some states are not available from the sensors. In addition, the key factor for estimation correction is the residual.

The convergence analysis is given in the Appendix. The multirate Kalman filter with residual compensation performs better than the one without compensation but behaves worse than the ideal case.

D. Kalman Gain Design

The performances of both single-rate and multirate Kalman filters rely on the adjustment of the Kalman gain, which is determined by Q and R. In this application, both Q and R are composed of vehicle-model-related and vision-model-related parts. As shown in (23), they are designed in diagonal forms

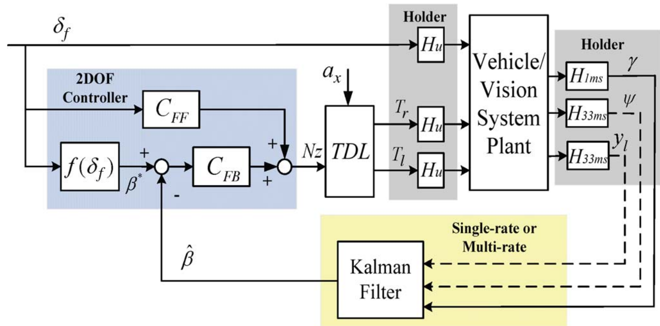

Fig. 6. Controller structure with body-slip-angle estimator.

to release the calculation burden. That is, the individual noise elements are assumed to be non-cross-related [21]

$$Q = \begin{bmatrix} Q^{veh} & 0 \\ 0 & Q^{\text{vis}} \end{bmatrix} \qquad R = \begin{bmatrix} R^{veh} & 0 \\ 0 & R^{\text{vis}} \end{bmatrix}. \tag{23}$$

The Kalman gain is calculated based on the degree by which the model and the measurements are weighted. Q represents the confidence placed on the observer model. If Q is set to be large, the estimates rely more on the measurements. R determines how much information from the measurements can be trusted, and the Kalman filter will follow the measurements more if R is smaller. Given that the system in this research is based on the combined model, the Q and R elements related to the different models need to be considered independently. For example, given that the vehicle model contains more uncertainties than the vision model, the elements of Q^{veh} are set to be relatively larger than those of Q^{vis}. The elements of R can be determined by offline analysis of the sensor signals [16], [21].

V. Body-Slip-Angle Controller Design Based on Estimation

The experimental vehicle employed in this study is small and light, but its body-slip-angle response is in the same level as the high-speed region of normal vehicles [17]. Therefore, implementing a control system that can manipulate the body slip angle to the desired value for handling and stability improvement is necessary. For traditional vehicles, active steering or differential braking is often employed as an actuator for lateral motion manipulation [13]. In the case of EVs with IWMs, the differential torque can be generated quickly and precisely by the left and right wheels, which can be effectively utilized for vehicle motion control. In this section, to achieve the goal of reference following, a 2DOF controller is designed with β feedback from a single-rate or multirate Kalman filter. The controller structure is shown in Fig. 6.

A. Desired Body Slip Angle

Based on the vehicle dynamic equations in (1) and (2), some studies calculate the reference body slip angle by assuming that a steady-state response is desired [2], [4].

Meanwhile, a desirable limit can be found on the body slip angle, and it changes under different road conditions [18]. Considering that drivers find it hard to recognize road conditions accurately, many vehicle stability control systems address the body-slip-angle control issue by preventing it from becoming too large [19]. Moreover, many traffic accidents occur because of excessive body slip angle [17]. For simplicity, this study assumes the desired slip angle to be zero [19]. That is, the reference body slip angle generated by $f(\delta_f)$ is zero.

TABLE II
Stability Margin Comparison

	Single-rate	Multi-rate
Closed-loop pole (Hz)	-2	-2
Gain Margin (dB)	5.92	22.8
Crossover Freq.(Hz)	15.15	477.46

B. Design of 2DOF Controller

As an effective method, the 2DOF controller is employed for reference tracking. This method consists of two parts: feedforward and feedback controllers. The feedforward controller is aimed at regulating the body slip angle to track the desired value. In this paper, the feedforward controller is designed as follows using the dc gains of the transfer functions from the body slip angle to the steering angle and yaw moment:

$$C_{FF} = \frac{G^{\beta}_{\delta_f}(0)}{G^{\beta}_{N_z}(0)} \cdot \delta_f = \frac{4l_r l C_f C_r - 2l_f C_f m V_x^2}{mV_x^2 + 2(l_f C_f - l_r C_r)} \cdot \delta_f. \tag{24}$$

To compensate for the modeling error and the error during transient operation, the feedback controller is indispensable. For information feedback, the body slip angle is estimated with either the single-rate or multirate Kalman filter. The estimated β is utilized as a feedback signal, and the proportional–integral controller C_{FB} is then designed based on pole placement. Together, the feedforward and feedback controllers generate the yaw moment for reference tracking.

On the one hand, the control period can be every 1 ms. On the other hand, the single-rate Kalman filter generates output every 33 ms, and the multirate Kalman filter is updated every 1 ms. Based on the parameters given in Table I and the open-loop stability analysis, the gain margins of the single-rate and multirate systems are given in Table II. As shown in Table II, the gain margin is increased by the multirate feedback. The multirate controller can provide smoother control input than the single-rate one [20]. Therefore, the controlled variable performs smoother in the case of multirate feedback compared with the single-rate feedback case, which can be observed later in the simulations and experiments.

After obtaining the desired yaw moment, torque commands of the left and right wheels can be distributed using the TDL introduced in Section II. Notably, the body-slip-angle controller here does not use a steering system and therefore can be independent from steering control. In addition, as can be observed in (3), the acceleration control and yaw moment control can be achieved independently. However, the torque commands cannot exceed motor limits.

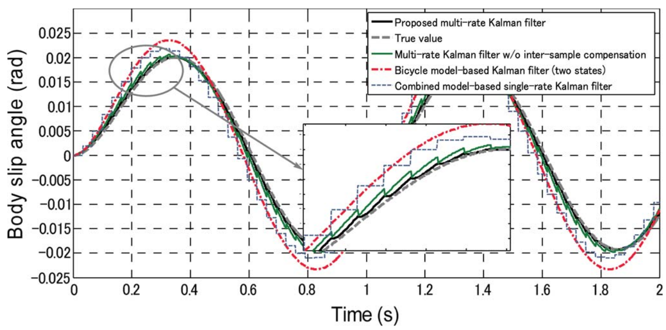

Fig. 7. Simulation comparison of the body-slip-angle estimation based on different estimation methods.

VI. Simulations and Experimental Results

A. Simulations

1) The performance of the proposed multirate Kalman filter was compared with the other methods based on the specifications in Table I. The vehicle was assumed to run at a speed of 25 km/h, and a sinusoidal steering input was given. To demonstrate clearly the effectiveness of the proposed method, the vehicle model and the Kalman filter model were made different from each other: The real C_f and C_r were set as 1.2 times larger than the estimator ones. A performance comparison among the bicycle-model-based Kalman filter, combined model-based single-rate Kalman filter, combined model-based multirate Kalman filter without intersample residual estimation, and the proposed method is shown in Fig. 7. The bicycle-model-based method cannot track the true value because of model discrepancy. The combined model-based single-rate estimator performed better because of the addition of visual information but was affected by slow update rate. The multirate estimator without intersample compensation exhibited better performance than the previous two methods; however, it cannot converge to the true value, as discussed in Section IV. Meanwhile, the proposed multirate Kalman filter with intersample compensation provided the best estimation result compared with the other methods.
2) Based on the analysis in Section IV, only the single-rate Kalman filter and the multirate Kalman filter with intersample residual compensation can converge, and both are more robust against vehicle parameter uncertainties than the bicycle-model-based method. The two methods were compared in the simulation with regard to the effect on control performance based on the controller in Section V. In the simulation, the vehicle was tested with a single-lane change maneuver at a speed of 25 km/h. For fair comparison, the gain margins of the two control system were set to be the same.

As shown in Fig. 8(a), the performance of the single-rate Kalman-filter-based controller is worse than that of the multirate Kalman-filter-based controller. In fact, the feedback gain in the case of the single-rate Kalman filter cannot be set large enough for reference tracking because of its low open-loop stability margin. In addition, the feedback gain in the case of the multirate estimator can be designed to track the reference. That is, the system stability margin is increased using the multirate Kalman filter as feedback.

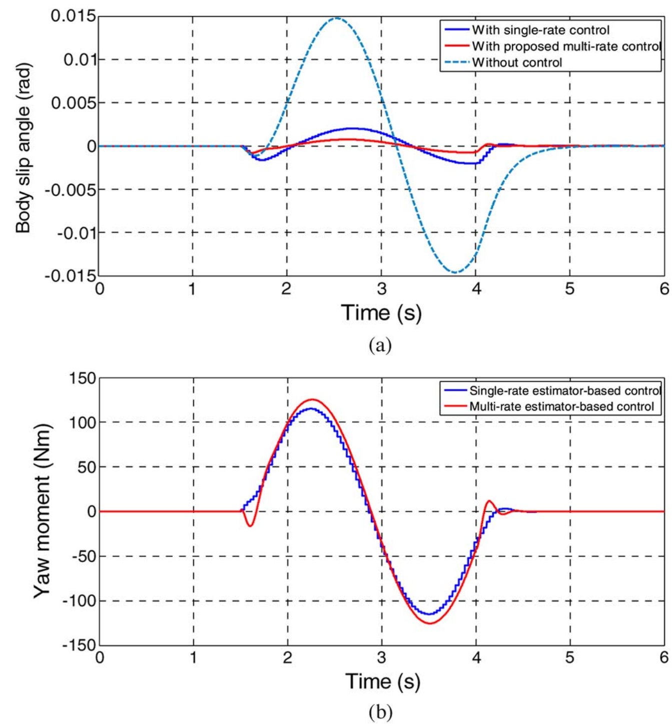

Fig. 8. Simulation comparison of the controller performances based on single-rate and multirate Kalman filters. (a) Body-slip-angle control comparison among the setup without control, single-rate estimator-based control, and proposed multirate control. (b) Yaw moment control input comparison between single-rate and multirate controllers.

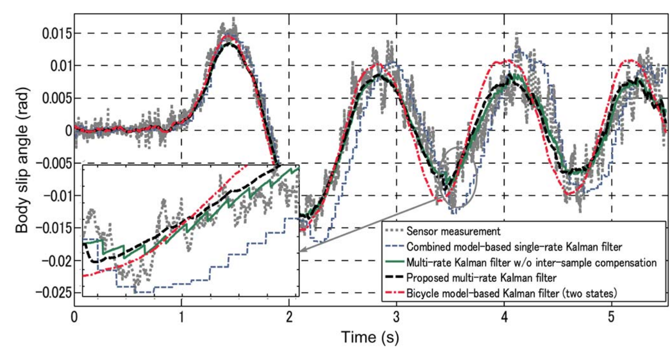

Fig. 9. Estimation method comparisons based on experimental data.

B. Experiments

1) Field tests were conducted with our experimental vehicle for realistic verification of the proposed estimator. A sinusoidal steering input was provided by the driver, and the vehicle speed varied from 0 to 30 km/h during the operation. Similar to the simulation settings, the C_f and C_r of the Kalman filter were made different from those of the real vehicle. In fact, the Kalman filter model was fixed in the experiment and could not be exactly the same with the vehicle. The proposed multirate observer was compared with the other methods (Fig. 9). The bicycle-model-based estimation result cannot track the true value

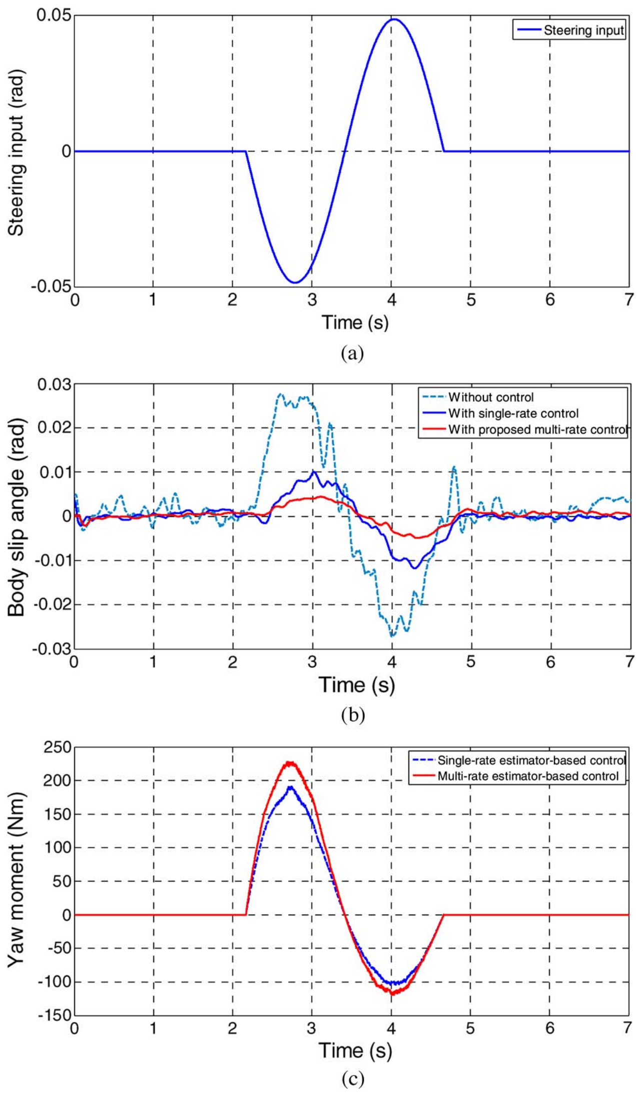

Fig. 10. Experimental comparison of the controller performance. (a) Steering input by EPS. (b) Body-slip-angle control comparison among the setup without control, single-rate estimator-based control, and the proposed multirate control. (c) Yaw moment control input comparison between the single-rate and multirate controllers.

very well because of model discrepancy. The combined model-based single-rate estimator was only updated at a rate of 30 Hz and was not able to utilize all the information from the fast-rate sensors. Hence, the estimation result was not satisfactory. In Fig. 9, the multirate Kalman filter without intersample compensation tracks the sensor measurement very well except for some vibrations at transient conditions. The proposed multirate estimator, which was compensated by intersample residuals, performed smoother and more accurately than the other methods.

2) Subsequently, the body-slip-angle controllers using either the single-rate or the proposed multirate Kalman filter were implemented and compared in the experiments. For fair comparison, a front-steering motor was employed to generate a single-lane change steering input with the same pattern. That is, the steering inputs were the same across all the experiments. The steering input is shown in Fig. 10(a). Based on the system sampling rate, both single-rate and multirate controllers were studied. As shown in Fig. 10(b), the amplitude of the body slip angle without control can reach almost 0.03 rad. With the single-rate controller, the body slip angle can be minimized, as illustrated by the blue dotted line. However, the feedback performance of such method deteriorated because of the low stability margin. Meanwhile, the body slip angle can be suppressed even further using the proposed multirate controller, as shown in Fig. 10(b). The control input, which is the yaw moment generated by the differential torque of the left and right wheels, is shown in Fig. 10(c).

VII. Conclusion

In this paper, a combined vehicle and vision model has been derived to increase the robustness of the body-slip-angle estimation against vehicle parameter uncertainties, and the multirate and time-delay issues have been explained. Then, the experimental vehicle and vision system setups have been introduced briefly. Based on the delay-augmented state space equation, intersample residual estimation and multirate Kalman filter with intersample compensation were designed and compared based on the estimation error analyses. Because of the intersample compensations, the proposed multirate Kalman filter with intersample residual estimation had the best estimation accuracy compared with the other methods. The 2DOF controller was designed for the desired β tracking using the estimated body slip angle. The proposed multirate estimator increased the open-loop stability margin compared with the single-rate one. Finally, simulations and experiments were conducted to verify the proposed estimator and controller. In addition to the application studied in this research, the proposed multirate estimator and controller can also be applied for enhanced lane-keeping control and vision-based robot control systems [7], [23].

Appendix
Convergence Analysis of Estimation Methods

The convergence of the ideal case (measurements are available at every short sampling time), the multirate Kalman filter without intersample residual compensation and the multirate Kalman filter with intersample residual compensation are analyzed.

1) Ideal Case: Considering the discrete Kalman filter given in (9), in the ideal case, measurements are available at every step, and the observation error at step $k+n$ is given as

$$\begin{aligned} e_{k+n} &= x_{k+n} - \hat{x}_{k+n} \\ &= G_{k+n-1} \cdot x_{k+n-1} + H_{k+n-1} \cdot u_{k+n-1} + w_{k+n-1} \\ &\quad - \overline{x}_{k+n} - K_{k+n} \cdot (y_{k+n} - C \cdot \overline{x}_{k+n}) \\ &= (I - K_{k+n} \cdot C) \cdot G_{k+n-1} \cdot e_{k+n-1} - K_{k+n} \cdot w_{k+n} \\ &\quad + (I - K_{k+n} \cdot C) \cdot w_{k+n-1} \\ &= \prod_{i=1}^{n} [(I - K_{k+i} \cdot C) \cdot G_{k+i-1}] \cdot e_k \end{aligned}$$

$$+\sum_{p=0}^{n-1}\left\{\prod_{i=p+1}^{n-1}\left[(I-K_{k+i+1}\cdot C)\cdot G_{k+i}\right]\cdot(I-K_{k+p+1}\cdot C)\cdot w_{k+p}\right\}$$
$$-\sum_{p=1}^{n}\left\{\prod_{i=p+1}^{n}\left[(I-K_{k+i}\cdot C)\cdot G_{k+i-1}\right]\cdot K_{k+p}\cdot v_{k+p}\right\}.$$

Obviously, well-designed Kalman gains perform n times to minimize the estimation error even if the system itself is unstable, and the subtraction of the measurement noise term v_{k+p} can further reduce the estimation error. That is, the estimation result can converge to true value gradually.

2) Multirate Kalman Filter Without Intersample Residual Compensation: In the case where measurements during intersamples are absent, the residuals are zero, and the observation error is derived as follows:

$$\begin{aligned}e_{k+n} &= x_{k+n}-\hat{x}_{k+n}\\ &= G_{k+n-1}\cdot x_{k+n-1}+H_{k+n-1}\\ &\quad\cdot u_{k+n-1}\cdot w_{k+n-1}-\overline{x}_{k+n}\\ &= G_{k+n-1}\cdot e_{k+n-1}+w_{k+n-1}\\ &= \prod_{i=0}^{n-1}(G_{k+i})\cdot e_k+\sum_{p=0}^{n-1}\left[\prod_{i=p+1}^{n-1}(G_{k+i})\cdot w_{k+p}\right].\end{aligned}$$

The error dynamic at step $k+n$ was found to be dependent only on the system matrix. That is, e_k+n is open loop.

3) Multirate Kalman Filter With Intersample Residual Compensation: To improve the convergence performance, the observation error was derived using the algorithm given in Section IV as follows:

$$\begin{aligned}e_{k+n} &= x_{k+n}-\hat{x}_{k+n}\\ &= G_{k+n-1}\cdot x_{k+n-1}+H_{k+n-1}\cdot u_{k+n-1}+w_{k+n-1}\\ &\quad-\overline{x}_{k+n}-K_{k+n}\cdot\tilde{\varepsilon}_{k+n}\\ &= G_{k+n-1}\cdot e_{k+n-1}+w_{k+n-1}-K_{k+n}\cdot\tilde{\varepsilon}_{k+n}\\ &= \prod_{i=0}^{n-1}(G_{k+i})\cdot e_k+\sum_{p=0}^{n-1}\left[\prod_{i=p+1}^{n-1}(G_{k+1})\cdot w_{k+p}\right]\\ &\quad-\sum_{p=1}^{n}\left[\prod_{i=p}^{n-1}(G_{k+1})\cdot K_{k+p}\cdot\tilde{\varepsilon}_{k+p}\right].\end{aligned}$$

Compared with the multirate Kalman filter without residual compensation in 2), the estimation error at step $k+n$ was subtracted by the estimated residual, which can reduce estimation error. That is, this method showed better convergence performance than the multirate Kalman filter without residual compensation. Meanwhile, the estimation error in this case can also be derived as

$$\begin{aligned}e_{k+n} &= x_{k+n}-\hat{x}_{k+n}\\ &= G_{k+n-1}\cdot e_{k+n-1}+w_{k+n-1}-K_{k+n}\cdot\tilde{\varepsilon}_{k+n}\\ &= G_{k+n-1}\cdot e_{k+n-1}+w_{k+n-1}-K_{k+n}\cdot C\\ &\quad\cdot G_{k+n-1}\cdot e_{k+n-1}\\ &= \prod_{i=1}^{n}\left[(I-K_{k+i}\cdot C)\cdot G_{k+i-1}\right]\cdot e_k\\ &\quad+\sum_{p=0}^{n-1}\left\{\prod_{i=p+1}^{n-1}\left[(I-K_{k+i+1}\cdot C)\cdot G_{k+i}\right]\cdot(I-K_{k+p+1}\cdot C)\cdot w_{k+p}\right\}.\end{aligned}$$

Compared with the ideal case in 1), the first two terms are the same. However, the measurement noise term is absent, which renders it worse than the ideal case.

References

[1] Y. Hori, "Future vehicle driven by electricity and control—Research on 4 wheel motored "UOT March II"," *IEEE Trans. Ind. Electron.*, vol. 51, no. 5, pp. 954–962, Oct. 2004.

[2] C. Geng, L. Mostefai, M. Denai, and Y. Hori, "Direct Yaw moment control of an in-wheel-motored electric vehicle based on body slip angle fuzzy observer," *IEEE Trans. Ind. Electron.*, vol. 56, no. 5, pp. 1411–1419, May 2009.

[3] A. T. van Zanten, "Bosch ESP systems: 5 years of experience," presented at the SAE Autom. Dynam. Stability Conf., Detroit, MI, USA, May, 2000, 2000-01-1633.

[4] Y. Aoki, T. Uchida, and Y. Hori, "Experimental demonstration of body slip angle control based on a novel linear observer for electric vehicle," in *Proc. 31st Annu. IEEE IECON*, Nov. 2005, pp. 6–10.

[5] C. Arndt, J. Karidas, and R. Busch, "Design and validation of a vehicle state estimator," in *Proc. AVEC*, 2004, pp. 41–45.

[6] G. Phanomchoeng, R. Rajamani, and D. Piyabongkarn, "Nonlinear observer for bounded Jacobian systems, with applications to automotive slip angle estimation," *IEEE Trans. Autom. Control*, vol. 56, no. 5, pp. 1163–1170, May 2011.

[7] J. C. McCall and M. M. Trivedi, "Video based lane estimation and tracking for driver assistance: Survey, system, and evaluation," *IEEE Trans. Intell. Transp. Syst.*, vol. 7, no. 1, pp. 20–37, Mar. 2006.

[8] S. Challa, R. Evans, and X. Wang, "A Bayesian solution and its approximations to out-of-sequence measurement problems," *J. Inf. Fusion*, vol. 4, no. 3, pp. 185–199, Sep. 2003.

[9] M. Moayedi, Y. K. Foo, and Y. C. Soh, "Adaptive Kalman filtering in networked systems with random sensor delays, multiple packet dropouts and missing measurements," *IEEE Trans. Signal Process.*, vol. 58, no. 3, pp. 1577–1588, Mar. 2010.

[10] V. Cerone, M. Milanese, and D. Regruto, "Experimental results on combined automatic lane keeping and driver's steering," in *Proc. Amer. Control Conf.*, Jul. 2007, pp. 3126–3131.

[11] L. Armesto, S. Chroust, M. Vincze, and J. Tornero, "Multi-rate fusion with vision and inertial sensors," in *Proc. IEEE Int. Conf. Robot. Autom.*, Apr. 2004, pp. 193–199.

[12] B. Bamieh, J. B. Pearson, B. A. Francis, and A. Tannenbaum, "A lifting technique for linear periodic systems with applications to sampled-data control," *Syst. Control Lett.*, vol. 17, no. 2, pp. 79–88, Aug. 1991.

[13] J. Yoon, W. Cho, B. Koo, and K. Yi, "Unified chassis control for rollover prevention and lateral stability," *IEEE Trans. Veh. Technol.*, vol. 58, no. 2, pp. 596–609, Feb. 2009.

[14] R. Wang and J. Wang, "Fault-tolerant control with active fault diagnosis for four-wheel independently driven electric ground vehicles," *IEEE Trans. Veh. Technol.*, vol. 60, no. 9, pp. 4276–4287, Nov. 2011.

[15] A. Smyth and M. Wu, "Multi-rate Kalman filtering for the data fusion of displacement and acceleration response measurements in dynamic system monitoring," *Mech. Syst. Signal Process.*, vol. 21, no. 2, pp. 706–723, Feb. 2007.

[16] K. Nam, H. Fujimoto, and Y. Hori, "Lateral stability control of in-wheel-motor-driven electric vehicles based on sideslip angle estimation using lateral tire force sensors," *IEEE Trans. Veh. Technol.*, vol. 61, no. 5, pp. 1972–1985, Jun. 2012.

[17] M. Shino and M. Nagai, "Independent wheel torque control of small-scale electric vehicle for handling and stability improvement," *JSAE Rev.*, vol. 24, no. 4, pp. 449–456, Oct. 2003.

[18] R. Rajamani, *Vehicle Dynamics and Control*. Berlin, Germany: Springer-Verlag, 2006, pp. 231–239.

[19] J. Song and W. S. Che, "Comparison and evaluation of brake yaw motion controllers with an antilock brake system," *Proc. IMechE, J. Autom. Eng.*, vol. 222, no. 7, pp. 1273–1288, Jul. 2008.

[20] H. Fujimoto and Y. Hori, "Visual servoing based on multirate sampling control," in *Proc. IEEE Int. Conf. Robot. Autom.*, 2001, pp. 711–716.

[21] K. Nam, S. Oh, H. Fujimoto, and Y. Hori, "Estimation of sideslip and roll angles of electric vehicles using lateral tire force sensors through RLS and Kalman filter approaches," *IEEE Trans. Ind. Electron.*, vol. 60, no. 3, pp. 988–1000, Mar. 2013.

[22] Y. Wang, B. M. Nguyen, P. Kotchapansompote, H. Fujimoto, and Y. Hori, "Vision-based vehicle body slip angle estimation with multi-rate Kalman filter considering time delay," in *Proc. IEEE ISIE*, May 2012, pp. 1506–1511.

[23] S. Y. Chen, J. Zhang, H. Zhang, N. M. Kwok, and Y. F. Li, "Intelligent lighting control for vision-based robotic manipulation," *IEEE Trans. Ind. Electron.*, vol. 59, no. 8, pp. 3254–3263, Aug. 2012.

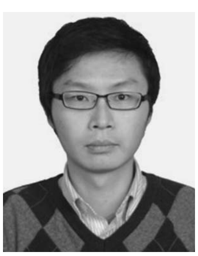

Yafei Wang (S'12) received the B.S. degree in internal combustion engines from Jilin University, Changchun, China, in 2005, the M.S. degree in vehicle engineering from Shanghai Jiao Tong University, Shanghai, China, in 2008, and the Ph.D. degree in electrical engineering from The University of Tokyo, Tokyo, Japan, in 2013.

From 2008 to 2010, he worked in the automotive industry, including an internship with FIAT Powertrain Technologies (Shanghai) and full-time working experience with the Delphi China Technical Center. He is currently a Postdoctoral Researcher with The University of Tokyo. He is interested in state estimation and control for electric vehicles, multirate estimation theory, and real-time image processing.

Binh Minh Nguyen (S'12) was born in Haiphong, Vietnam. He received the M.S. degree in electrical engineering from The University of Tokyo, Tokyo, Japan, in 2012, where he is currently working toward the Ph.D. degree in the Department of Advanced Energy, Graduate School of Frontier Sciences.

His current research interests include state estimation and motion control of electric vehicles, application of GPS in vehicle motion control, and robust control theory.

Hiroshi Fujimoto (S'99–M'01–SM'13) received the Ph.D. degree from the Department of Electrical Engineering, The University of Tokyo, Tokyo, Japan in 2001.

In 2001, he joined Nagaoka University of Technology, Nagaoka, Japan, as a Research Associate. From 2002 to 2003, he was a Visiting Scholar in the School of Mechanical Engineering, Purdue University, West Lafayette, IN, USA. In 2004, he joined the Department of Electrical and Computer Engineering, Yokohama National University, Yokohama, Japan, as a Lecturer, where he became an Associate Professor in 2005. Since 2010, he has been an Associate Professor with The University of Tokyo. His interests are in control engineering, motion control, nanoscale servo systems, electric vehicle control, and motor drives.

Dr. Fujimoto is a member of the Institute of Electrical Engineers of Japan, the Society of Instrument and Control Engineers (SICE), the Robotics Society of Japan, and the Society of Automotive Engineers of Japan. He was the recipient of the Best Paper Award from the IEEE TRANSACTIONS ON INDUSTRIAL ELECTRONICS in 2001, the Isao Takahashi Power Electronics Award in 2010, and the Best Author Prize of SICE in 2010.

Yoichi Hori (S'81–M'83–SM'00–F'05) received the B.S., M.S., and Ph.D. degrees in electrical engineering from The University of Tokyo, Tokyo, Japan, in 1978, 1980, and 1983, respectively.

In 2000, he became a Professor at The University of Tokyo, where he has been with the Department of Advanced Energy, Graduate School of Frontier Sciences, since 2008. His research fields are control theory and its industrial applications to motion control, mechatronics, robotics, electric vehicles, etc.

Prof. Hori was the President of the Industry Applications Society of the Institute of Electrical Engineers of Japan, the President of the Capacitors Forum, the Chairman of the Motor Technology Symposium of the Japan Management Association, and the Director of Technological Development of the Society of Automotive Engineers of Japan. He was the recipient of the Best Transactions Paper Award from the IEEE TRANSACTIONS ON INDUSTRIAL ELECTRONICS in 1993 and 2001 and the 2011 Achievement Award of the Institute of Electrical Engineers of Japan.